Acta Polytechnica **65**(4):467–477, 2025
https://doi.org/10.14311/AP.2025.65.0467

Published by the Czech Technical University in Prague

MATHEMATICAL MODELLING AND ANALYSIS OF THREE-DIMENSIONAL MAXWELL-NANOFLUID FLOW OVER A BIDIRECTIONAL STRETCHING SURFACE IN THE PRESENCE OF A MAGNETIC FIELD

Tanuku Poornakantha[a], Mamidi Lakshmi Prasanna[b], Murali Gundagani[c,*]

[a] *Gayatri Vidya Parishad College of Engineering for Women, 530048 Visakhapatnam, India*
[b] *Andhra University, Trans-Disciplinary Research Hub, 530003 Visakhapatnam, India*
[c] *Geethanjali College of Engineering and Technology, 501301 Cheeryal, India*
[*] corresponding author: prof.murali20@gmail.com

Abstract. The current study investigates the effects of thermal diffusion and diffusion thermoeffect on three-dimensional upper-convected Maxwell-Nanofluid flow across a bidirectional stretching surface in the presence of Brownian motion, thermophoresis, and thermal and mass Biot numbers. The current communication is also being carried out to consider the unique and innovative properties of nanofluids. The Rosseland approximation incorporates a nonlinear radiative heat flow in the energy equation. By adding applicable dimensionless variables and parameters, the governing equations are converted into a dimensionless form and then solved via finite element system. The paper delivers a comprehensive analysis of how various factors and other pertinent parameters influence the flow variables. These findings are presented visually through graphical representations, providing a clear and insightful understanding involved in this flow scenario. The results obtained demonstrate that it is an effective solution to the current problem. This new research has significant implications for the food industry, as well as for energy systems, biomedical engineering, and aeronautics. The numerical findings of this investigation are tangible and validated.

Keywords: Maxwell fluid, three-dimensional, nanofluid, magnetic field, thermal Biot number, mass Biot number, finite element method.

1. Introduction

It is critical to include radiative heat flow while studying heat transfer processes, especially in regard to nanofluids. Radiative heat transfer is carried out using electromagnetic waves throughout the energy transmission process. Heat transmission properties can be adjusted further in the presence of nanofluids, which are liquid suspensions containing microscopic particles. Radiative heat transfer has traditionally been described using linear models such as the Stefan-Boltzmann equation that assume a linear relationship between the temperature difference and the radiative heat flow. In some cases, a non-linear radiative heat flow model can be better suited to accurately portray the behaviour of heat transfer. The addition of a non-linear radiative heat flow compensates for the radiative properties of the nanofluid, including the scattering and absorption of radiation by the nanoparticles floating in the fluid. These variables can influence radiative heat transfer by altering the fluid's effective thermal conductivity, as well as its absorption and emission properties. There are many approaches that can be applied to describe the non-linear radiative heat flow in the presence of a nanofluid. Nanoparticle concentration, size, and shape are all widely included in radiative heat transfer estimates. This is made feasible by using complex mathematical models or numerical simulations that account for the interactions between the nanoparticles and the incoming radiation. The extinction coefficient and scattering phase function of the nanofluid, as well as other radiative properties, can be determined through experiments. In order to make more accurate forecasts, these observable characteristics can then be included into non-linear radiative heat transfer models. A fluid is a unique form of matter with the ability to flow and deform easily when subjected to an external force. Non-Newtonian fluids have innumerable real-life applications in natural products, bio-medical fields, agriculture, and food products. Exhaustive benefits in various fields have made researchers to study and investigate the attributes of non-Newtonian fluids. The non-Newtonian liquid stream has received a lot of attention over the past 10 years due to its wide range of applications in the engineering and industrial sectors. A key type of rate-based liquid model is the Maxwell liquid. The straightforward rate-based fluid subclass for which the analytical solution can be reasonably anticipated or obtained is the Maxwell fluid model. Several academics have examined the Maxwell liquid stream past various geometries in this area. In recent years, modelling and exploration of nanoliquid

streams has been a popular area of study. Nanoliquids are being offered as a breakthrough approach to increase heat transmission. One of the technological applications of nanoparticles is the use of heat transfer liquids including nanoparticle suspensions to overcome cooling difficulties in thermal frames. As a result, numerous researchers examined the nanoliquid stream as it passed through various surfaces. Because of their complicated rheology, certain fluids cannot be represented by simple Navier-Stokes equations. Non-Newtonian fluids have various uses in our daily lives, including biotechnologies, geophysics, astrophysics, industries, and engineering innovations.

The nonlinear radiative heat transfer properties of nanofluids with varying parameters were studied by Chamkha and Abu-Nada [1]. An exhaustive survey of studies on non-linear radiative heat transport in nanofluids was conducted by Chandrasekar and Suresh [2]. The radiative heat transport characteristics of nanofluids were studied by Cheng [3]. The non linear radiative heat transfer investigation of nanofluids in a curved tube was the main focus of the work of Huminic et al. [4]. Karimipour et al. investigated the radiative heat transfer in nanofluids using the extended Mie theory [5]. The primary focus of Liu and Zhang's research was nanofluid nonlinear radiative heat transfer [6]. Molaali et al. investigated nonlinear radiative heat transfer in a cavity comprising porous media saturated with a nanofluid [7]. Murthy and Devi offered an overview of non-linear radiative heat transfer studies in nanofluids that takes shifting thermal conductivity and viscosity into consideration [8]. Rashidi and Tavakolpour-Saleh investigated non-linear radiative heat transfer in a nanofluid-filled inclined lid-driven cavity [9]. Rashidi et al. investigated the nonlinear radiative heat transfer in a lid-driven square cavity filled with a nanofluid composed of several types of nanoparticles [10]. Roslan et al. comprehensively analysed radiation heat transfer in nanofluids [11]. Sadeghinezhad and Chamkha investigated the nonlinear radiative heat transfer in nanofluid-filled microchannels with different cross-sectional shapes [12]. Sadri, Esfahani, and Afrand investigated the non-linear radiative heat transfer of a CuO-MWCNT/water hybrid nanofluid in a porous media [13]. Selimefendigil and Ztop investigated natural convection utilising nonlinear radiation in a nanofluid-filled container [14]. Vafaei et al. investigated nonlinear radiative heat transfer in nanofluids containing nanoparticles of various shapes [15]. Xu et al. investigated non-linear radiation heat transfer in nanofluids using a two-phase model [16]. Zhang et al. investigated how radiation affects natural convection in a square cage containing a nanofluid [17]. Zhang and Zheng published a novel theory for non-linear radiation heat transfer in nanofluids [18]. N. V. N. Babu et al. studied the Heat and mass transfer effects and their findings had a significant impact on understanding the nature of radiative heat transfer in nanofluids [19–23]. S. A. A. Shah et al. studied the effects of convection on the flow of a Prandtl hybrid nanofluid with a chemical reaction and motile microorganisms over a stretching sheet [24]. Numerous significant investigations undertaken in this domain are included in the references [25–28].

According to a study of the works described above, relatively few studies have documented the three-dimensional analysis of nanofluid flow in the presence of a magnetic field and a non-radiative heat flux. No reports on the combined effects of thermal diffusion (Soret) and diffusion thermoeffect (Dufour) on steady, three-dimensional, incompressible, viscous, electrically conducting, non-Newtonian upper-convected Maxwell-Nanofluid flow over a bi-directional stretching sheet (surface) in the presence of non-linear radiative heat flux, Brownian motion, Thermophoresis, thermal, and mass Biot numbers, have yet been published in the literature. This model is an enhanced version of a previously published research. The outcomes of the current numerical simulations are also different.

2. Mathematical formulation

This section covers the effects of thermophoresis, Brownian motion, thermal diffusion, and the diffusion thermoeffect on three-dimensional, steady, incompressible, viscous, non-Newtonian Maxwell fluid flow over a bidirectional stretching. The shape of the fluid flow is shown in Figure 1.

The following premises are assumed in order to undertake this inquiry:

(1.) It is thought that the magnetic Reynolds number should be as low as possible in order to ignore the generated magnetic field.

(2.) It is presumed that the sheet moves at velocities $U_w(x) = ax$ and $V_w(y) = by$ along the x and y axes, respectively.

(3.) In this study, the flow is subjected to a magnetic field with a strength of Bo.

(4.) Ohmic heating, viscous dissipation, heat source, and joule heating effects are neglected in the energy equation and the effects of Thermophoresis, Brownian motion, and Dufour effects are assumed in the energy equation.

(5.) In the species concentration equation, the effect of thermal diffusion is considered and chemical reaction effect is neglected.

(6.) Let T_w be the constant temperature and T_∞ the fluid temperature exterior to the thermal boundary layer.

(7.) The convective boundary condition is used when the surface of a sheet is heated by a hot fluid with a uniform temperature T_f, concentration φ_f, convective heat transfer coefficient β_1 and mass transfer coefficient β_2.

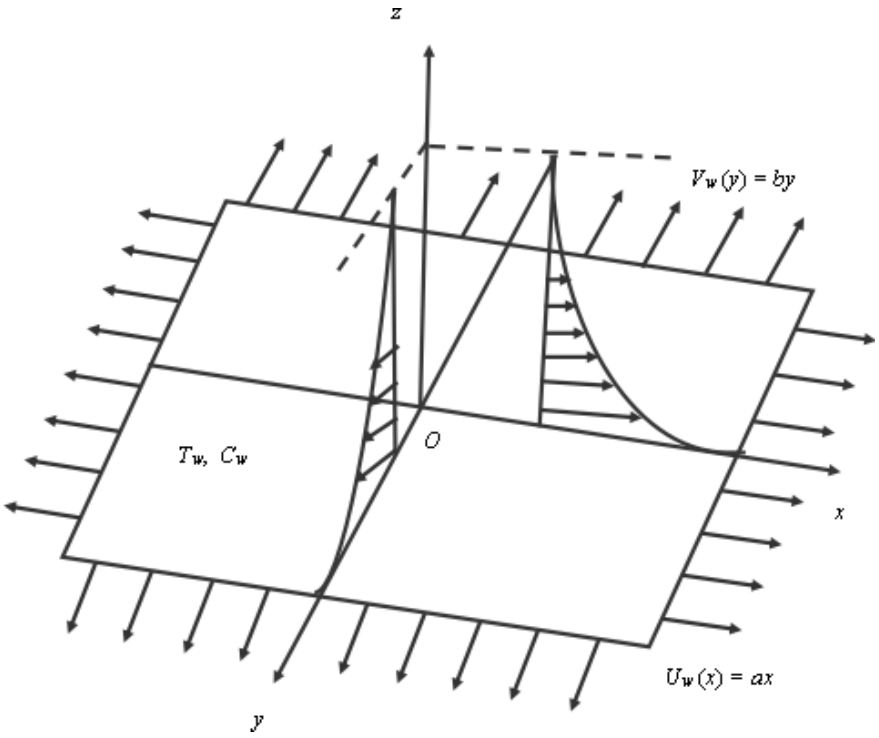

FIGURE 1. Graphical representation of Nano-Maxwell fluid flow.

The equation for continuity:

$$\frac{\partial u}{\partial x}+\frac{\partial v}{\partial y}+\frac{\partial w}{\partial z}=0. \tag{1}$$

Momentum equation:

$$\begin{aligned}&u\left(\frac{\partial u}{\partial x}\right)+v\left(\frac{\partial u}{\partial y}\right)+w\left(\frac{\partial u}{\partial z}\right)\\&+\lambda\left\{\begin{array}{c}u^2\left(\frac{\partial^2 u}{\partial x^2}\right)+v^2\left(\frac{\partial^2 u}{\partial y^2}\right)\\+w^2\left(\frac{\partial^2 u}{\partial z^2}\right)+2uv\left(\frac{\partial^2 u}{\partial x\partial y}\right)\\+2vw\left(\frac{\partial^2 u}{\partial y\partial z}\right)+2uw\left(\frac{\partial^2 u}{\partial x\partial z}\right)\end{array}\right\}\\&=\frac{\partial^2 u}{\partial z^2}-\left(\frac{\sigma B_o^2}{\rho}\right)u,\end{aligned} \tag{2}$$

$$\begin{aligned}&v\left(\frac{\partial v}{\partial x}\right)+v\left(\frac{\partial v}{\partial y}\right)+w\left(\frac{\partial v}{\partial z}\right)\\&+\lambda\left\{\begin{array}{c}v^2\left(\frac{\partial^2 v}{\partial x^2}\right)+v^2\left(\frac{\partial^2 v}{\partial y^2}\right)\\+w^2\left(\frac{\partial^2 v}{\partial z^2}\right)+2uv\left(\frac{\partial^2 v}{\partial x\partial y}\right)\\+2vw\left(\frac{\partial^2 v}{\partial y\partial z}\right)+2uw\left(\frac{\partial^2 v}{\partial x\partial z}\right)\end{array}\right\}\\&=\frac{\partial^2 v}{\partial z^2}-\left(\frac{\sigma B_o^2}{\rho}\right)v.\end{aligned} \tag{3}$$

Equation of thermal energy:

$$\begin{aligned}&u\left(\frac{\partial T}{\partial x}\right)+v\left(\frac{\partial T}{\partial y}\right)+w\left(\frac{\partial T}{\partial z}\right)\\&=\alpha\left(\frac{\partial^2 T}{\partial z^2}\right)\\&+\left(\frac{(\rho C)_p}{(\rho C)_f}\right)\left\{D_B\left(\frac{\partial T}{\partial z}\right)\left(\frac{\partial \varphi}{\partial z}\right)+\frac{D_T}{T_\infty}\left(\frac{\partial T}{\partial z}\right)^2\right\}\\&-\frac{1}{\rho C_p}\left(\frac{\partial q_r}{\partial z}\right)+\frac{D_m K_T}{C_s C_p}\left(\frac{\partial^2 \varphi}{\partial z^2}\right).\end{aligned} \tag{4}$$

Equation of species concentration:

$$\begin{aligned}&u\left(\frac{\partial \varphi}{\partial x}\right)+v\left(\frac{\partial \varphi}{\partial y}\right)+w\left(\frac{\partial \varphi}{\partial z}\right)\\&=D_B\left(\frac{\partial^2 \varphi}{\partial z^2}\right)+\frac{D_T}{T_\infty}\left(\frac{\partial T}{\partial z}\right)^2+\frac{D_m K_T}{T_m}\left(\frac{\partial^2 T}{\partial y^2}\right).\end{aligned} \tag{5}$$

The following are the flow boundary conditions:

$$\left.\begin{aligned}&u=U_w=ax,\ v=V_w=by,\ w=0,\\&-\kappa\frac{\partial T}{\partial z}=\beta_1\left(T_f-T\right),\\&-D_B\frac{\partial C}{\partial z}=\beta_2\left(\varphi_f-\varphi\right)atz=0,\\&u\to 0,\ v\to 0,\ T\to T_\infty,\ \varphi\to\varphi_\infty asz\to\infty.\end{aligned}\right\} \tag{6}$$

The radiative heat flux (using Roseland approximation) is defined as:

$$q_r=-\frac{4\sigma^*}{3K^*}\left(\frac{\partial T^4}{\partial z}\right), \tag{7}$$

$$T^4=T_\infty^4+4T_\infty^3\left(T-T_\infty\right)+6T_\infty^2\left(T-T_\infty\right)^2+\ldots \tag{8}$$

After disregarding higher-order terms after the first degree term $(T - T_\infty)$, we get:

$$T^4 \cong 4T_\infty^3 T - 3T_\infty^4. \tag{9}$$

From (7) and (9), we get:

$$q_r = -\frac{16T_\infty^3 \sigma^*}{3K^*}\left(\frac{\partial T}{\partial z}\right). \tag{10}$$

Using (8), Equation (3) can be written as:

$$\begin{aligned} &u\left(\frac{\partial T}{\partial x}\right) + v\left(\frac{\partial T}{\partial y}\right) + w\left(\frac{\partial T}{\partial z}\right) \\ &= \alpha\left(\frac{\partial^2 T}{\partial z^2}\right) \\ &+ \left(\frac{(\rho C)_p}{(\rho C)_f}\right)\left\{D_B\left(\frac{\partial T}{\partial z}\right)\left(\frac{\partial C}{\partial z}\right) + \frac{D_T}{T_\infty}\left(\frac{\partial T}{\partial z}\right)^2\right\} \\ &+ \frac{1}{\rho C_p}\left(\frac{16T_\infty^3\sigma^*}{3\kappa k^*}\right)\left(\frac{\partial^2 T}{\partial z^2}\right) + \frac{D_m K_T}{C_s C_p}\left(\frac{\partial^2 C}{\partial z^2}\right). \end{aligned} \tag{11}$$

The following similarity transformations are initiated:

$$\left.\begin{aligned} &\eta = \left(\sqrt{\frac{a}{\nu}}\right) z,\ u = axf'(\eta),\ v = ayg'(\eta), \\ &\theta = \frac{T - T_\infty}{T_f - T_\infty},\ \phi = \frac{\varphi - \varphi_\infty}{\varphi_f - \varphi_\infty}, \\ &w = \nu\sqrt{\nu a}\{f(\eta) + g(\eta)\}. \end{aligned}\right\} \tag{12}$$

Via these transformations (12), Equations (2), (3), (4) and (11) take the following form:

$$\begin{aligned} &f''' - f'^2 + ff'' + gf'' - Mf' \\ &\quad + K\left\{2ff'f'' + 2gf'f'' - (f+g)^2 f'''\right\} = 0, \\ &g''' - g'^2 + fg'' + gg'' - Mg' \\ &\quad + K\left\{2fg'g'' + 2gg'g'' - (f+g)^2 g'''\right\} = 0, \\ &\left\{\frac{d}{d\eta}\left[\left(1 + R\left(1 + (\theta_w - 1)\theta\right)^3\right)\theta'\right]\right\} + Prf\theta' \\ &\quad + Prg\theta' + PrNb\theta'\phi' + PrNt\theta'^2 \\ &\quad + PrDu\phi'' = 0, \\ &Nb\phi'' + NbScf\phi' + NbScg\phi' + Nt\theta'' \\ &\quad + ScNbSr\theta'' = 0. \end{aligned}$$

The associated boundary conditions (6) become:

$$\left.\begin{aligned} &f(0) = 0,\ g(0) = 0,\ f'(0) = 1,\ g'(0) = C, \\ &\theta'(0) = -\delta(1 - \theta(0)),\ \phi'(0) = -\zeta(1 - \phi(0)), \\ &f'(\infty) \to 0,\ g'(\infty) \to 0,\ \theta(\infty) \to 0,\ \phi(\infty) \to 0. \end{aligned}\right\}$$

Where the involved physical parameters are defined as:

$$\left.\begin{aligned} &M = \frac{\sigma B_o^2}{\rho U_o},\ K = \lambda_1 a,\ C = \frac{b}{a},\ \theta_w = \frac{T_w}{T_\infty}, \\ &Nb = \frac{\tau_B D_B(\varphi_f - \varphi_\infty)}{\nu},\ Pr = \frac{\nu}{\alpha},\ \delta = \frac{\beta_1}{\kappa}\sqrt{\frac{\nu}{a}}, \\ &\zeta = \frac{\beta_2}{D_B}\sqrt{\frac{\nu}{a}},\ Nt = \frac{\tau_B D_T(T_f - T_\infty)}{\nu T_\infty}, \\ &Sr = \frac{D_m K_T(T_f - T_\infty)}{T_m \nu(\varphi_f - C_\infty)},\ Du = \frac{D_m K_T(\varphi_f - \varphi_\infty)}{C_s C_p \nu(T_f - T_\infty)}, \\ &Sc = \frac{\nu}{D_B},\ R = \frac{16\sigma^* T_\infty^3}{3\kappa k^*}. \end{aligned}\right\} \tag{13}$$

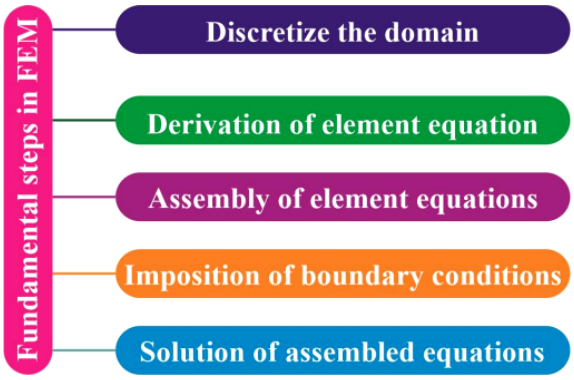

Figure 2. Fundamental steps in the finite element method.

The physical parameters are presented as follows:

$$\begin{aligned} C_{fx} &= \frac{\tau_{wx}}{\rho U_w^2} = \frac{1}{\rho U_w^2}\mu\left(\frac{\partial u}{\partial y}\right)_{y=0} \\ &\Rightarrow C_{fx} = C_{fx}\left(\sqrt{Re_x}\right) = f''(0), \end{aligned} \tag{14}$$

$$\begin{aligned} C_{fy} &= \frac{\tau_{wy}}{\rho V_w^2} = \frac{\mu}{\rho V_w^2}\left(\frac{\partial v}{\partial y}\right)_{y=0} \\ &\Rightarrow C_{fy} = C_{fy}\left(\sqrt{Re_y}\right) = g''(0), \end{aligned} \tag{15}$$

$$\begin{aligned} Nu &= \frac{xq_w}{\kappa(T_f - T_\infty)} = -\frac{x\left(\frac{\partial T}{\partial y} + \frac{\partial q_r}{\partial y}\right)_{y=0}}{\kappa(T_f - T_\infty)} \\ &\Rightarrow Nu = -\left(1 + R\theta_w^3\right)\left(\sqrt{Re_x}\right)\theta'(0), \end{aligned} \tag{16}$$

$$\begin{aligned} Sh &= \frac{xq_m}{D_B(C_f - C_\infty)} = -\frac{x\left(\frac{\partial C}{\partial y}\right)_{y=0}}{D_B(C_f - C_\infty)} \\ &\Rightarrow Sh = -\left(\sqrt{Re_x}\right)\phi'(0), \end{aligned} \tag{17}$$

$$Re_x = \frac{u_x(x)\,x}{\nu}, \tag{18}$$

$$Re_y = \frac{v_w(y)\,y}{\nu}. \tag{19}$$

Based on the stretching velocities, the local Reynolds numbers (18) and (19) have shown.

3. Methods

Numerical models are developed that perfectly match the physical system, enabling the solutions to be analysed and compared with the real system. These numerical methods enable us to refine our approach to the physical system and solve it quickly. The following are the advantages of the FEM technique:

- Modelling,
- adaptability,
- accuracy,
- boundaries,
- visualisation.

The core procedural stages of the finite element method was shown in Figure 2. The finite element

C	Present numerical results			Results of Ammar Mushtaq et al. [29]		
	$-f''(0)$	$-g''(0)$	$-\theta'(0)$	$-f''(0)$	$-g''(0)$	$-\theta'(0)$
0.25	1.0385679834	0.1867437347	0.6545640347	1.048811	0.194564	0.665926
0.50	1.0826347693	0.4560274634	0.7210683909	1.093095	0.465205	0.735333
0.75	1.1286789826	0.7826707660	0.7820676830	1.134486	0.794618	0.796472
1.00	1.1668398949	1.1668398949	0.8425687981	1.173721	1.173721	0.851992

TABLE 1. Comparison of present numerical results with those published by Ammar Mushtaq et al. [29] for various values of C at $Pr = 1.0$ when $M = 0$, $Nb = 0$, $Nt = 0$, $Sr = 0$, $Du = 0$, $\zeta \to \infty$ and $\delta \to \infty$.

C	Present numerical results			Results of Liu and Anderson [30]		
	$-f''(0)$	$-g''(0)$	$-\theta'(0)$	$-f''(0)$	$-g''(0)$	$-\theta'(0)$
0.25	1.0286896981	0.1850897908	0.6477834499	1.048813	0.194565	0.665933
0.50	1.0798579345	0.4487475729	0.7188967643	1.093096	0.465206	0.735334
0.75	1.1183468884	0.7798774410	0.7776784938	1.134486	0.794619	0.796472

TABLE 2. Comparison of present numerical results with those published by Liu and Anderson [30] for various values of C at $Pr = 1.0$ when $M = 0$, $K = 0$, $R = 0$, $Nb = 0$, $Nt = 0$, $Sr = 0$, $Du = 0$, $\zeta \to \infty$ and $\delta \to \infty$.

method used in this study is a highly useful approach for solving linear and nonlinear partial and ordinary differential equations in physics, mechanical engineering, and related subjects, and can therefore be used in future research. At the time this article was written, this was the most adaptable numerical technique available for carrying out engineering analysis. Numerous numerical techniques, including the LU decomposition approach and the Gauss elimination method, can be used to solve the built equations.

These approaches are most commonly used to solve built equations. When working with real numbers, it is important to remember that form functions can be used to provide an accurate approximation of real functions. If you follow this technique step by step, you can be certain that your calculations will be accurate. The flow domain has the total of 20 001 nodes and is divided into 10 000 quadratic components that are all of the same size. These components are all of the same shape. The flow domain is made up of 10 000 quadratic components, all of which are of the same magnitude as their counterparts in the other components. Following the development of the element equation, a total of 80 004 nonlinear equations could be investigated. These equations were made available for study.

After applying the boundary conditions, the Gauss approach was used to eliminate the remaining nonlinear equations. The Gauss technique was then employed to obtain an accurate numerical solution to within 0.00001 degrees. Gaussian quadrature is used to help overcome the challenges associated with integration.

The custom software for the method was run on a desktop computer within the context of a suitable programming environment. The software was developed specifically for the method. MATHEMATICA is the name of the programming language that was used to create the software application for the computer.

3.1. Program code validation

Tables 1 and 2 compare the authors' most recent numerical findings for various values of C at $Pr = 1.0$ with those previously reported by Liu and Anderson [30] and Ammar Mushtaq et al. [29]. This comparison demonstrates the close alignment between our numerical findings and the results of published studies.

4. Results and discussion

In this section, the authors have created a series of images to illustrate the potential impact of various factors on equations for temperature, concentration, and dimensionless velocity. The parameter ranges necessary to generate the graphical representations are built on the following critical values: M (Magnetic field parameter) = 0.5, K (Maxwell fluid parameter or Deborah number) = 0.5, C (Velocity ratio parameter) = 0.5, Pr (Prandtl number) = 0.22, $R = 0.5$, $Nb = 0.5$, $Nt = 0.5$, Du (Dufour number) = 0.5, Sr (Soret number) = 0.5, Sc (Schmidt number) = 0.22, δ (Thermal Biot number) = 0.1, ζ (Mass Biot number) = 0.1, and θ_w (Temperature ratio parameter) = 0.5 (see Figures 3–20). Figures 3 and 4 show the effect of the magnetic field parameter (M) on the velocity profiles along x- and y- directions, respectively. It has been demonstrated that velocity fields diminish as M increases. The fluid flow tends to slow down in the presence of a magnetic field, which reduces the thickness of the velocity and momentum boundary layers. The influence of the Maxwell fluid parameter, or Deborah number (K), on the x- and y-

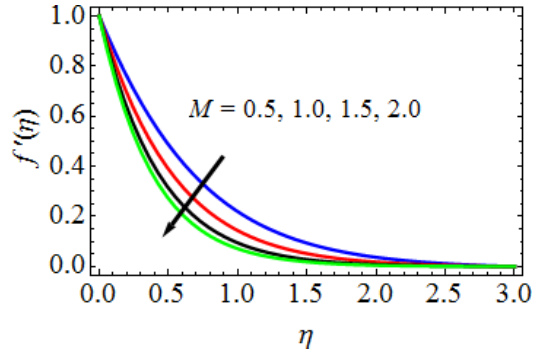

Figure 3. Primary velocity profile sensitivity to magnetic field parameter.

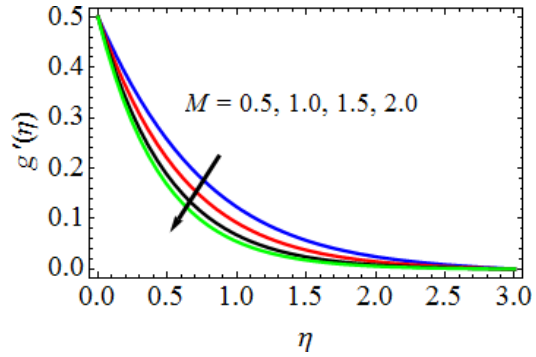

Figure 4. Secondary velocity sensitivity to magnetic field parameter.

components of velocity is sketched in the Figures 5 and 6 respectively.

The deviation of the fluid's relaxation period from its basic timescale is quantified by the Deborah number. The relaxation period is the amount of time the fluid requires to reach equilibrium following the application of the shear force. It is predicted that higher viscosity fluids may take longer to relax. Since fluid viscosity slows down fluid motion and decreases velocity, it is possible to interpret an increase in K in this way. As K increases, the hydrodynamic boundary layer becomes thinner. It should also be noted that the three-dimensional flow exhibits a greater shift in the velocity fields f and g than the axisymmetric and two-dimensional flows. Figures 7 and 8 illustrate the behaviour of the velocity ratio parameter (C) on the primary and secondary velocity profiles, respectively. These figures show that both the primary and secondary velocity profiles increase with rising values of the velocity ratio parameter.

Figure 9 illustrates how the Prandtl number changes with temperature. It can be concluded that increasing Prandtl number values produce narrower temperature boundary layers. Temperatures drop as a result of reduced thermal diffusivity in fluids with higher Prandtl numbers. The variations in temperature profiles caused by an increase in the values of (R) are shown in Figure 10. Because the conduction effect of the nanofluid increases in the presence of R, the fluid temperature rises as R increases. Larger values of R

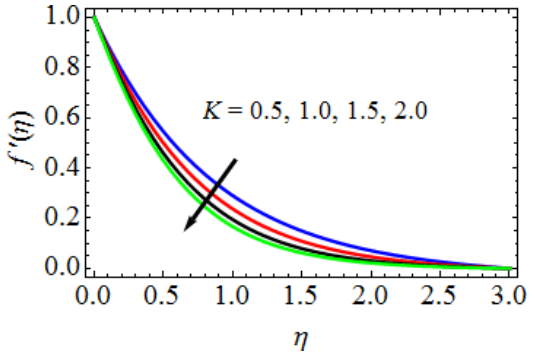

Figure 5. Primary velocity profile sensitivity to Maxwell fluid parameter.

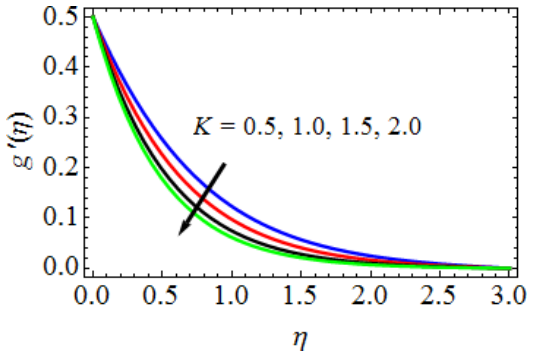

Figure 6. Secondary velocity profile sensitivity to Maxwell fluid parameter.

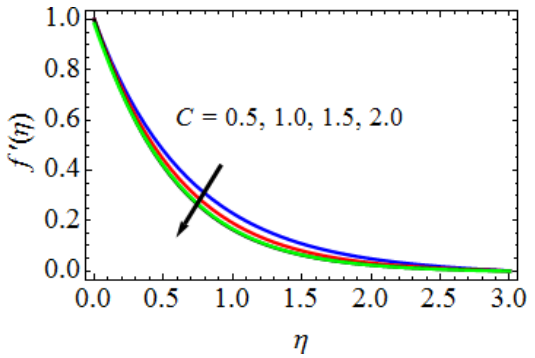

Figure 7. Primary velocity profile sensitivity to velocity ratio parameter.

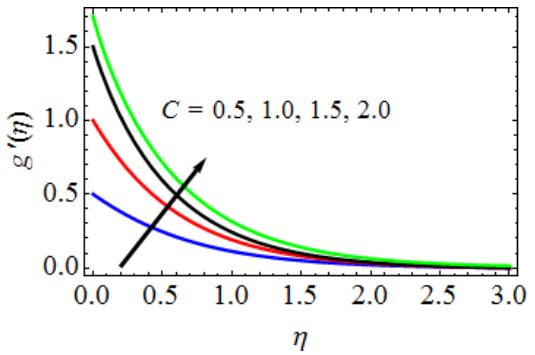

Figure 8. Velocity profiles along y- direction.

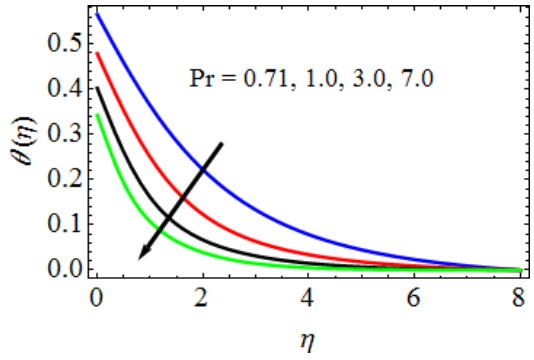

FIGURE 9. Temperature for different values of Pr.

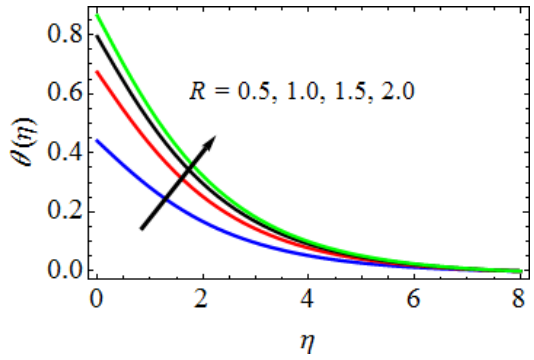

FIGURE 10. Temperature profiles for various values of R.

thus imply greater surface heat transfer, raising the temperature in the vicinity of the boundary layer.

Figures 11 and 12 clearly illustrate this fact: as the values of the Brownian motion parameter increase, the thermal boundary layer thickens and the temperature difference at the surface decreases. However, the concentration profiles and concentration boundary layer thickness exhibit the opposite tendency when the Brownian motion parameter increases. The effect of the thermophoresis parameter (Nt) on temperature and concentration curves can be seen in Figures 13 and 14.

These findings demonstrate that the temperature and concentration boundary layer thickness increases as the thermophoresis parameter grows. Contrasting Figures 15 and 16 clearly shows how the Dufour number (Du) and the Soret number (Sr) vary in relation to the temperature and concentration profiles. Physically, Du has to do with how a concentration gradient affects the thermal energy of a liquid. Increasing Sr values also improves concentration profiles, much like increasing Sr levels do. This is because, when there is a temperature gradient, mass can move more easily from an area of lower solute concentration to an area of higher concentration. How the Schmidt number (Sc) impacts the concentration profiles can be seen in Figure 17.

The Sc value is a representation of the mass diffusivity to momentum ratio. It is possible to evaluate the relative importance of momentum and mass transfer using diffusion in the concentration (species) bound-

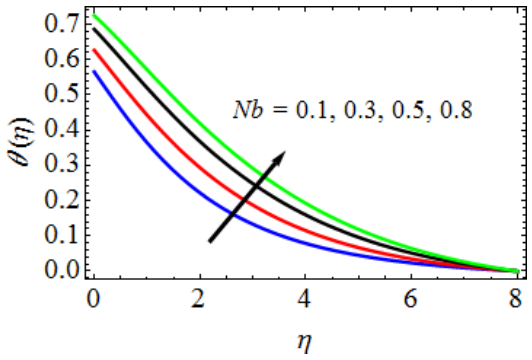

FIGURE 11. Temperature distributions for various values of Nb.

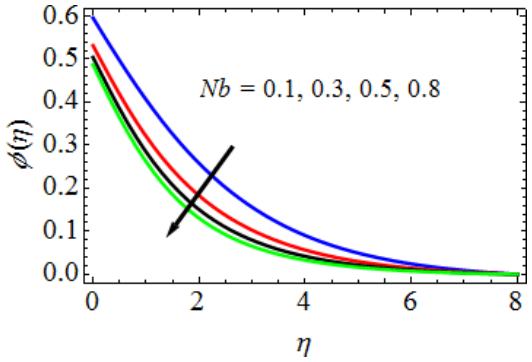

FIGURE 12. Concentration distributions for various values of Nb.

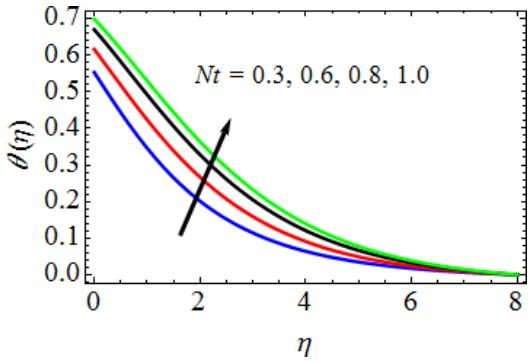

FIGURE 13. Temperature distributions for various values of Nt.

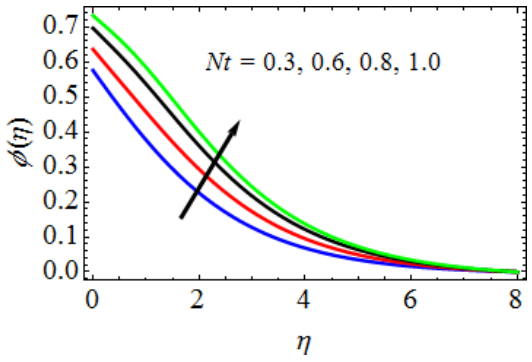

FIGURE 14. Concentration distributions for various values of Nt.

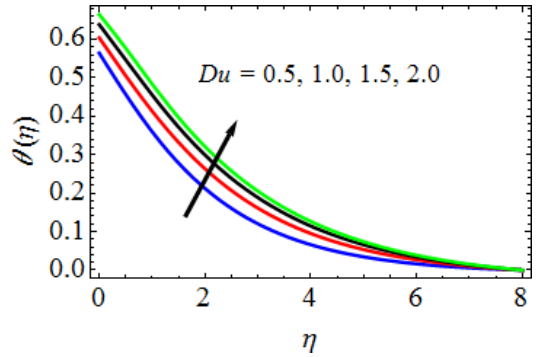

Figure 15. Temperature distributions for various values of Du.

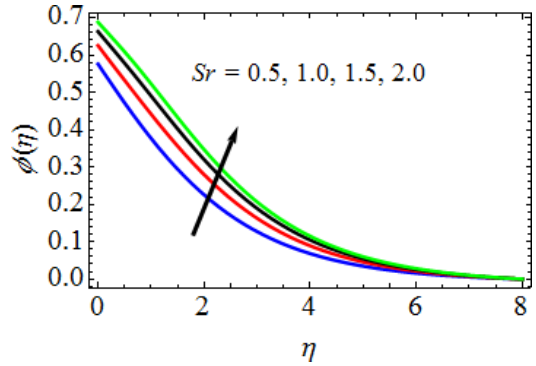

Figure 16. Concentration distributions for various values of Sr.

ary layer. A decrease in the fluid's mass diffusivity is brought on by a higher Sc value due to the inverse relationship between mass diffusivity and Sc value. Weaker concentration boundary layers are actually linked to a higher Sc concentrations. The temperature field's impact on the thermal Biot number is shown in Figure 18. With an increase, convection intensifies, raising the temperature field. As can be seen from Figure 19, concentration profiles increase as the mass Biot number increases. From Figure 20, it can be seen that a larger value of θ_w corresponds to a higher temperature and a thicker thermal boundary layer. As the coefficient of the latter component, parameter θ_w is therefore expected to support the thermal boundary layer thickness. Further observation reveals that the profiles take on a unique S-shaped structure as θ_w increases, proving the presence of an adiabatic scenario. In other words, when the ratio of the wall temperature to the ambient temperature is sufficient enough, the wall temperature gradient approaches zero.

It was noted that the skin friction coefficients along the x and y axes (C_{fx} and C_{fy}, respectively) increase with increasing values of C (velocity ratio parameter), R, Nb, Nt, Du, Sr, δ, ζ, θ_w (temperature ratio parameter) and decrease with increasing values of M, K (Maxwell fluid parameter or Deborah number), Pr, and Sc.

As can be seen from Table 3, the heat transfer coefficient rate increases with rising values of R, Nb, Nt, Du, and δ, θ_w while the opposite effect is observed

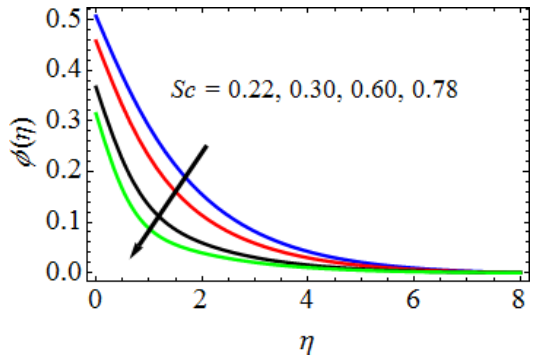

Figure 17. Concentration profiles for various values of Sc.

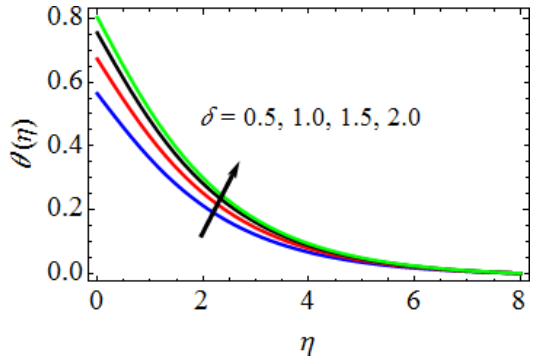

Figure 18. Temperature distributions for various values of δ.

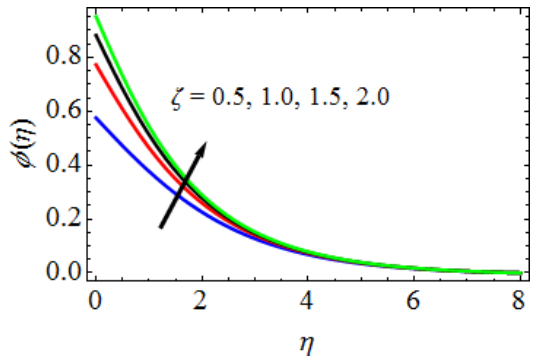

Figure 19. Concentration profiles for various values of ζ.

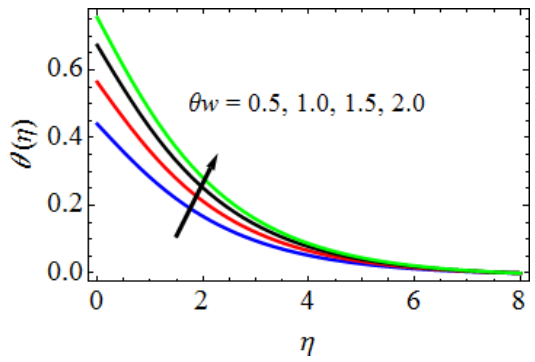

Figure 20. Temperature profiles for various values of θ_w.

Pr	R	Nb	Nt	Du	δ	θ_w	Nu_x
0.71	0.5	0.1	0.3	0.5	0.5	0.5	1.596830981948893
1.00							1.540146983497358
7.00							1.522678298079871
	1.0						1.622579819879815
	1.5						1.640867673619807
		0.3					1.611567987134682
		0.5					1.632676708713469
			0.6				1.621674784390873
			0.8				1.643657036096307
				1.0			1.629676710760369
				1.5			1.646783093109616
					1.0		1.612669136036737
					1.5		1.633676846987895
						1.0	1.609561387560034
						1.5	1.620561387408763

TABLE 3. Results for the rate of heat transfer coefficient.

with Pr. As shown in Table 4, the mass transfer coefficient rate increases with growing values of the Nt, Sr, and ζ, while dropping with rising values of the Nb and the Schmidt number.

5. Conclusion

An extensive numerical parametric study was performed on a class of nonlinear equations to provide a detailed numerical explanation of the solution and deliver a comprehensive analysis of how various factors, including the nanofluid properties and other pertinent parameters, influence the flow variables. These findings are presented visually through graphical representations, providing a clear and insightful understanding of the results of this study. The resulting conclusions are:

- Thermal radiation, thermophoresis, Brownian motion, Dufour number, thermal Biot number, and temperature ratio are all indicators of rising temperature profiles.
- The concentration profiles decrease as the Schmidt number, a Brownian motion parameter, increases.
- The temperature profiles decrease as the Prandtl number increase.
- As the values of the Maxwell fluid and magnetic field parameters increase, the velocity profiles in the x and y directions decrease, however, the velocity ratio parameter has the opposite effect.
- When the values of the thermophoresis parameter, the Soret number, and the mass Biot number values increase, the concentration profiles expand.
- Finally, under certain conditions, the current numerical results closely align with the those published by Ammar Mushtaq et al. [29] and Liu and Anderson [30].

Nt	Nb	Sc	Sr	ζ	Sh_x
0.3	0.1	0.22	0.5	0.5	1.865613746076340
0.6					1.899564701676437
0.8					1.921696347687664
	0.3				1.838673618736870
	0.5				1.810136763487613
		0.30			1.835639609613409
		0.78			1.817561348760834
			1.0		1.889365871387687
			1.5		1.909567613476763
				1.0	1.890563467630197
				1.5	1.915673413847891

TABLE 4. Results for the rate of mass transfer coefficient.

5.1. Future research directions

The finite element method used in the current study is a highly useful approach to solving linear and nonlinear partial and ordinary differential equations in physics, mechanical engineering, and other related subjects, and can therefore be used in future research. The resulting findings are more accurate than those obtained using other numerical approaches. The finite element method is currently employed by mechanical engineers to solve complex problems. To improve our understanding of transport phenomena, temperature profiles, and concentration profiles, future research must examine the characteristics of nanofluid flow.

References

[1] E. Abu-Nada, A. J. Chamkha. Mixed convection flow of a nanofluid in a lid-driven cavity with a wavy wall. *International Communications in Heat and Mass Transfer* **57**:36–47, 2014. https://doi.org/10.1016/j.icheatmasstransfer.2014.07.013

[2] M. Chandrasekar, S. Suresh. A review on the mechanisms of heat transport in nanofluids. *Heat*

Transfer Engineering **30**(14):1136–1150, 2009. https://doi.org/10.1080/01457630902972744

[3] C. Peng, L.-P. Wang. Direct numerical simulations of turbulent pipe flow laden with finite-size neutrally buoyant particles at low flow Reynolds number. *Acta Mechanica* **230**(2):517–539, 2019. https://doi.org/10.1007/s00707-018-2268-2

[4] G. Huminic, A. Huminic. Heat transfer and flow characteristics of conventional fluids and nanofluids in curved tubes: A review. *Renewable and Sustainable Energy Reviews* **58**:1327–1347, 2016. https://doi.org/10.1016/j.rser.2015.12.230

[5] A. Karimipour, A. Taghipour, A. Malvandi. Developing the laminar MHD forced convection flow of water/FMWNT carbon nanotubes in a microchannel imposed the uniform heat flux. *Journal of Magnetism and Magnetic Materials* **419**:420–428, 2016. https://doi.org/10.1016/j.jmmm.2016.06.063

[6] Q. Zhao, Y. Lei, H. Jin, et al. Numerical simulation of flow and heat transfer performance during supercritical water injection in vertical wellbore: A parameter sensitivity analysis. *International Journal of Thermal Sciences* **183**:107855, 2023. https://doi.org/10.1016/j.ijthermalsci.2022.107855

[7] H. Vaidya, K. V. Prasad, F. Mebarek-Oudina, et al. Heat and mass transfer characteristics in peristaltic transport of temperature-dependent Eyring Powell nanofluid through an inclined uniform channel. *International Journal of Ambient Energy* **46**(1):2503271, 2025. https://doi.org/10.1080/01430750.2025.2503271

[8] P. V. S. N. Murthy, M. F. El-Amin. Thermo-diffusion effect on free convection heat and mass transfer in a thermally linearly stratified non-Darcy porous media. *The Open Transport Phenomena Journal* **3**:49–55, 2011. https://doi.org/10.2174/1877729501103010049

[9] S. Rashidi, M. Akbarzadeh, R. Masoodi, E. M. Languri. Thermal-hydraulic and entropy generation analysis for turbulent flow inside a corrugated channel. *International Journal of Heat and Mass Transfer* **109**:812–823, 2017. https://doi.org/10.1016/j.ijheatmasstransfer.2017.02.033

[10] S. Rashidi, M. Eskandarian, O. Mahian, S. Poncet. Combination of nanofluid and inserts for heat transfer enhancement. *Journal of Thermal Analysis and Calorimetry* **135**(1):437–460, 2019. https://doi.org/10.1007/s10973-018-7070-9

[11] R. Roslan, H. Saleh, I. Hashim. Buoyancy-driven heat transfer in nanofluid-filled trapezoidal enclosure with variable thermal conductivity and viscosity. *Numerical Heat Transfer, Part A: Applications* **60**(10):867–882, 2011. https://doi.org/10.1080/10407782.2011.616778

[12] E. Sadeghinezhad, H. Togun, M. Mehrali, et al. An experimental and numerical investigation of heat transfer enhancement for graphene nanoplatelets nanofluids in turbulent flow conditions. *International Journal of Heat and Mass Transfer* **81**:41–51, 2015. https://doi.org/10.1016/j.ijheatmasstransfer.2014.10.006

[13] R. Sadri, G. Ahmadi, H. Togun, et al. An experimental study on thermal conductivity and viscosity of nanofluids containing carbon nanotubes. *Nanoscale Research Letters* **9**(1):151, 2014. https://doi.org/10.1186/1556-276X-9-151

[14] F. Selimefendigil, H. F. Öztop, A. J. Chamkha. MHD mixed convection and entropy generation of nanofluid filled lid driven cavity under the influence of inclined magnetic fields imposed to its upper and lower diagonal triangular domains. *Journal of Magnetism and Magnetic Materials* **406**:266–281, 2016. https://doi.org/10.1016/j.jmmm.2016.01.039

[15] S. Vafaei, T. Borca-Tasciuc, D. Wen. Theoretical and experimental investigation of quasi-steady-state bubble growth on top of submerged stainless steel nozzles. *Colloids and Surfaces A: Physicochemical and Engineering Aspects* **369**(1–3):11–19, 2010. https://doi.org/10.1016/j.colsurfa.2010.07.009

[16] X. Xu, C. Guan, L. Xu, et al. Three dimensionally free-formable graphene foam with designed structures for energy and environmental applications. *ACS Nano* **14**(1):937–947, 2020. https://doi.org/10.1021/acsnano.9b08191

[17] X. Zhang, G. Ahmadi. Numerical simulations of gas-liquid-particle flows in three-phase slurry reactors under gravity variation. *Scientia Iranica B* **25**(6):3197–3209, 2018. https://doi.org/10.24200/sci.2018.20892

[18] X. Zhang, G. Ahmadi. Numerical simulations of liquid-gas-solid three-phase flows in microgravity. *The Journal of Computational Multiphase Flows* **4**(1):41–63, 2012. https://doi.org/10.1260/1757-482X.4.1.41

[19] D. Gadipally, M. Gundagani. Analysis of Soret and Dufour effects on unsteady MHD convective flow past a semi-infinite vertical porous plate via finite difference method. *International Journal of Applied Physics and Mathematics* **4**(5):332–344, 2014. https://doi.org/10.7763/IJAPM.2014.V4.306

[20] N. V. N. Babu, A. Paul, M. Gundagani. Soret and Dufour effects on unsteady hydromagnetic free convective fluid flow past an infinite vertical porous plate in the presence of chemical reaction. *Journal of Science and Arts* **15**(1):99–111, 2015.

[21] G. Murali, A. Paul, N. V. N. Babu. Heat and mass transfer effects on an unsteady hydromagnetic free convective flow over an infinite vertical plate embedded in a porous medium with heat absorption. *International Journal of Open Problems in Computer Science and Mathematics* **8**(1):15–27, 2015. https://doi.org/10.12816/0010706

[22] M. Gundagani, S. Sheri, A. Paul, M. C. K. Reddy. Radiation effects on an unsteady MHD convective flow past a semi-infinite vertical permeable moving plate embedded in a porous medium with viscous dissipation. *Walailak Journal of Science and Technology (WJST)* **10**(5):499–515, 2013.

[23] M. Gundagani, N. V. N. Babu. Convective MHD Jeffrey fluid flow due to vertical plates with pulsed fluid suction: Numerical study. *Journal of Computational Applied Mechanics* **54**(1):36–48, 2023. https://doi.org/10.22059/jcamech.2023.351326.773

[24] S. A. A. Shah, N. A. Ahammad, E. M. T. El Din, et al. Bio-convection effects on Prandtl hybrid nanofluid flow with chemical reaction and motile microorganism over a stretching sheet. *Nanomaterials* **12**(13):2174, 2022. https://doi.org/10.3390/nano12132174

[25] M. Gundagani, N. V. N. Babu, D. Gadially, et al. Study of Nano-Powell-Erying fluid flow past a porous stretching sheet by the effects of MHD, thermal and mass convective boundary conditions. *Journal of Umm Al-Qura University for Engineering and Architecture* **15**(3):271–281, 2024. https://doi.org/10.1007/s43995-024-00056-2

[26] M. Gundagani, D. Gadially, V. Nirmala Kasturi, T. Poornakantha. Joint effects of thermal diffusion and diffusion thermo on MHD three dimensional nanofluid flow towards a stretching sheet. *Mathematical Models in Engineering* **9**(4):130–143, 2023. https://doi.org/10.21595/mme.2023.23590

[27] M. Gundagani, L. P. Mamidi, P. K. Tanuku. Finite element solutions of double diffusion effects on three-dimensional MHD Nano-Powell-Erying fluid flow in presence of thermal and mass Biot numbers. *Journal of Engineering and Applied Science* **71**(1):9, 2024. https://doi.org/10.1186/s44147-023-00347-w

[28] P. K. Tanuku, L. P. Mamidi, M. Gundagani. Modelling and analysis of three-dimensional chemically reacting, radiating Casson-nanofluid flow: Thermophoresis and Brownian motion effects. *Acta Polytechnica* **64**(5):455–463, 2024. https://doi.org/10.14311/AP.2024.64.0455

[29] A. Mushtaq, M. Mustafa, T. Hayat, A. Alsaedi. A numerical study for three-dimensional viscoelastic flow inspired by non-linear radiative heat flux. *International Journal of Non-Linear Mechanics* **79**:83–87, 2016. https://doi.org/10.1016/j.ijnonlinmec.2015.11.006

[30] I.-C. Liu, H. I. Andersson. Heat transfer over a bidirectional stretching sheet with variable thermal conditions. *International Journal of Heat and Mass Transfer* **51**(15–16):4018–4024, 2008. https://doi.org/10.1016/j.ijheatmasstransfer.2007.10.041